Donor End-capped Alkyl Chain Length Dependent Non-Radiative Energy Loss in All-small-molecule Organic Solar Cells

*Lili Zhang,[#] Rui Sun,[#] Ziqi Zhang, Jianqi Zhang, Qinglian Zhu, Wei Ma, Jie Min, Zhixiang Wei and Dan Deng **

Ms. L. L. Zhang, Mr. Z. Q. Zhang, Dr. J. Q. Zhang, Prof. Z. X. Wei, Dr. D. Deng,

CAS Key Laboratory of Nanosystem and Hierarchical Fabrication, CAS Center for Excellence in Nanoscience, National Center for Nanoscience and Technology, Beijing 100190, China

Ms. L. L. Zhang,

Sino-Danish Center for Education and Research, Sino-Danish College, University of Chinese Academy of Sciences, Beijing 100049, China

Mr. R. Sun; Prof. J. Min,

The Institute for Advanced Studies, Wuhan University, Wuhan 430072, China

Mr. Q. L. Zhu; Prof. W. Ma,

State Key Laboratory for Mechanical Behavior of Materials, Xi'an Jiaotong University, Xi'an 710049, China.

*Correspondence: dengd@nanoctr.cn

This is the author manuscript accepted for publication and has undergone full peer review but has not been through the copyediting, typesetting, pagination and proofreading process, which may lead to differences between this version and the Version of Record. Please cite this article as doi: 10.1002/adma.202207020.

Keywords: end-capped alkyl chains, organic solar cells, condense packing, non-radiative voltage loss, thermal annealing

Abstract: A fatal bottleneck for further efficiency breakthroughs in organic solar cells (OSCs) is to minimize the non−radiative energy loss (eΔV_{nr}) while maximizing the charge generation. With the development of highly emissive low−bandgap nonfullerene acceptors, the design of high−performance donors becomes critical to enable the blend with the electroluminescence quantum efficiency to approach or surpass the pristine acceptor. Herein, by shortening the end−capped alkyl chains of the small molecular donors from hexyl (MPhS−C6) to ethyl (MPhS−C2), the material obtained insensitive aggregation to thermal annealing (TA) and condensed packing simultaneously. The former led to small phase separation and suppressed upshifts of HOMO energy level during TA, and the latter facilitated its efficient charge transport at aggregation−less packing. Hence, the ΔV_{nr} decreases from 0.242 to 0.182 V, from MPhS−C6 to MPhS−C2 based OSCs. An excellent PCE of 17.11% was obtained by DIO addition due to almost unchanged high J_{sc} (26.6 mA cm^{-2}) and V_{oc} (0.888 V) with improved FF, which is the record efficiency with the smallest energy loss (0.497 eV) and ΔV_{nr} (0.192V) in ASM−OSCs. Our results emphasize the potential material design direction of obtaining concurrent TA−insensitive aggregation and condensed packing to maximize the device performances with a super low ΔV_{nr}.

1. Introduction

Organic solar cells (OSCs) have made significant progress by using non-fullerene acceptors, with power conversion efficiency (PCE) surpassing 19% in single-junction cells and 20% in tandem cells.[1-5] The invention of the highly emissive non−fullerene acceptors (NFAs), especially the ITIC and Y-series

acceptors,[6-9] reduced the voltage loss in the near-infrared absorption (NIR) system successfully, which alleviated the dilemma of open−circuit voltage (V_{oc}) and short circuit current (J_{sc}) in fullerene systems.[10] The mechanism could be well explained by the equilibrium between the charge transfer (CT) states, and highly emissive local excited (LE) states due to a small $\Delta E_{LE\text{-}CT}$ (the energy disparity between LE and CT states). The smaller $\Delta E_{LE\text{-}CT}$ leads to a shift of the CT–LE equilibrium towards the LE states of the emissive acceptor material, leading to a lower non-radiative energy loss ($e\Delta V_{nr}$).[11-13] However, the $\Delta E_{LE\text{-}CT}$ also acts as the driving force for charge generation [14, 15], and therefore, the smaller $\Delta E_{LE\text{-}CT}$, the less efficient charge generation may occur. Hence, the fatal bottleneck still exists for further breakthroughs in the device performance of OSCs, and that is how to minimize non-radiative losses while maximizing the efficient charge generation.

In highly emissive NFAs−based OSCs, the external electroluminescence quantum efficiency (EQE_{EL}) of the blends exhibits several orders of magnitude disparity for different donors, and it is also much lower than that of the pristine acceptor. As indicated by the equation of ΔV_{nr} ($\Delta V_{nr} \approx (-k_b T/q)\ln(EQE_{EL})$), the ΔV_{nr} could be much lower if the EQE_{EL} of the blends could be increased. As Nelson *et al.* have pointed out,[11] the very low ΔV_{nr} could be attained but may come at the cost of higher overall recombination rates, thus lower fill factor (FF) and short circuit current (J_{sc}) for highly hybridized systems; and an ideal morphology has the potential to improve the FF and J_{sc}. Vandewal *et al.* observed a less aggregated blend morphology resulting from the low molecular weight of PM6, decreasing the ΔV_{nr} from 0.250 to 0.177 eV; however, the PCE decreased from 15.4% to 7.6% with dramatically reduced FF and J_{sc}.[16] The CT state is related to both charge generation and ΔV_{nr}, but it could be easily and highly influenced by the interfacial morphology and molecular packing ability.[17-19] Hence, it is challenging to design donors to enable an optimized blend morphology to obtain simultaneous low ΔV_{nr} and efficient charge generation, which is critical to maximizing the value of ($V_{oc} \times J_{sc}$) and device performances.

All small molecule OSCs (ASM−OSCs), composed of the small−molecule donor and small−molecule acceptor, have great potential for future application because of their superior materials and device repeatability as a result of their definite molecular structure.[20-24] Furthermore, the power conversion efficiency (PCE) of the binary and ternary ASM−OSCs have surpassed 16%[25] and 17%, [26] respectively. However, the optimized device performances are usually obtained through post−treatment, such as thermal annealing (TA), which is an important loss channel of ΔV_{nr}.[27, 28] Consequently, an aggregation-insensitive to post-treatment aspect should be taken into account in the donor design in ASM−OSCs. Moreover, to alleviate the side effect of TA−insensitive aggregation on the hole mobility, condensed π−π stacking need to be further introduced for the material design. By carefully considering the common morphology requirements of efficient charge generation, charge transport and low ΔV_{nr}, we convert the donor design strategy to obtain the molecules with small phase separation, condense stacking and TA−insensitive aggregation.

In this contribution, based on our previously reported high-efficient donor material M-PhS, we shortened the end−capped alkyl chains from hexyl to butyl to ethyl and synthesized three donor materials of **MPhS−C6**, **MPhS−C4**, and **MPhS−C2 (Figure 1a)**. Compared to **MPhS−C6**, **MPhS−C2** exhibited a smaller driving force for molecular packing in the film and condenser packing. Using BTP−eC9 as an acceptor, a bulk heterojunction with small phase separation, tight molecular packing, and suppressed upshifts of HOMO energy levels to TA was formed, leading to a PCE of 16.54% with efficient charge generation (J_{sc} of 26.86 mA cm^{-2}) and a low ΔV_{nr} of 0.182 V (V_{oc} of 0.886 V). Significantly, a high EQE_{EL} was achieved in the optimized blend of MPhS-C2/BTP−eC9 without any additives, which was more than eight times higher than that of its corresponding pristine acceptor. Further, the addition of 1, 8−diiodoctane (DIO) improved the hole mobility, leading to a record PCE of 17.11% with a small energy loss of 0.497 eV in ASM−OSCs. Our results suggest that obtaining condense and TA−insensitive molecular packing would be an efficient donor material design direction to achieve high J_{sc} and V_{oc} simultaneously.

2. Results and discussions

2.1. Design and characterization of small donors

The synthesis routes and detailed procedures of the small molecules are shown in Scheme S1 and Synthesis Procedure in the Supporting Information (SI). The absorption spectrums of the three small molecules completely coincide with each other in chloroform (CF) solution, and **MPhS**−**C4** exhibits a slightly blue−shifted absorption band edge and a lower shoulder peak intensity in the solid states compared to that of **MPhS**−**C6** and **MPhS**−**C2 (Figure 1b)**, due to their slightly differed molecular packing. The highest occupied molecular orbital (HOMO) and lowest occupied molecular orbital (LUMO) energy levels were calculated from the onset oxidation (E_{OX}) and reduction (E_{RE}) potentials (**Figure 1c**), which were obtained from the measurement of cyclic voltammetry (CV, **Figure S1**). The calculated HOMO energy levels were −5.35, −5.39, and −5.35 eV for **MPhS**−**C2**, **MPhS**−**C4**, and **MPhS**−**C6**, respectively, and their corresponding LUMO energy levels are −3.45, −3.43 and −3.43 eV, respectively. Anyway, the similar HOMO energy levels of the small molecules (especially for **MPhS**−**C2** and **MPhS**−**C6**) rule out the influence of the initial HOMO energy level on their variation of V_{oc}.

An efficient charge generation is inseparable from the small domain size. The driving force of phase separation is a combined effect of miscibility and crystallinity.[25, 29] Due to the strong miscibility between our previously reported highly efficient **MPhS**−**C6** and BTP−eC9, hence, shortening its end-capped alkyl chains from hexyl (**MPhS**−**C6**) to butyl (**MPhS**−**C4**) to ethyl (**MPhS**−**C2**), retains its strong miscibility during film formation. The strong miscibility could be supported by their similar surface energy and Flory−Huggins interaction parameter χ with BTP-eC9

(**Figure 1d**, **Figure s2**, and **Table s1**), and χ values were 0.35, 0.34, and 0.29 for **MPhS**−**C6/BTP**−**eC9**, **MPhS**−**C4/BTP**−**eC9**, and **MPhS**−**C2/BTP**−**eC9**, respectively.

Shorter chains decrease the space between molecular backbones, thus reducing the molecular mobility and rotation space during the heating trace,[30] probably leading to a less aggregation sensitivity to TA, which is our original design of the small donors. To evaluate the TA aggregation sensitivity of the molecules, the driving forces (ΔG_{ls}) of crystallinity in their film were calculated by using the function of $\Delta G_{ls} = -\Delta H_m/T_m\ (T_m - T_c)$, where ΔH_m , T_m, and T_c represent enthalpy change during melting, melting point, and crystallinity temperature during cooling, respectively. The first scan of differential scanning calorimetry (DSC) was used for the calculation.[31, 32] As shown in **Figure 1e** and **Table *S2***, the long alkyl chain decreased the T_m, but exhibited slightly stronger molecular interactions;[33] however, shortening the end-capped alkyl chains significantly increased the T_c, and they were 170.7, 160.0, and 125.7 °C for **MPhS**−**C2**, **MPhS**−**C4,** and **MPhS**−**C6**, respectively. Consequently, the corresponding calculated ΔG_{ls} had a big difference, and they were −5.29, −7.04, and −12.68 J/g, respectively. Generally, a larger Gibbs energy variation illustrated a more temperature-sensitive aggregation. Hence, shortening end−capped alkyl chain length efficiently lowered the ΔG_{ls}, which would lead to a temperature−insensitive aggregation. Furthermore, the aggregation insensitivity of **MPhS**−**C2** to TA, together with strong miscibility between **MPhS**−**C2** and BTP−eC9 would also ensure a small phase separation.

The aggregation-insensitivity to TA has effects on molecular packing, and thus, grazing incidence wide−angle X−ray scattering (GIWAXS) was performed. The 2−dimensional (2D) GIWAX images and corresponding 1−dimensional (1D) curves are shown in **Figures S3**−**4**, and the detailed parameters are summarized in **Table S3.** As shown in **Figures 2a**−**b**, the differences among the three donors in stacking capacity widen significantly after TA. In the in-plane (IP) direction, the CCL increment of (010) is -0.02, 10.36, and 7.71 Å for **MPS**−**C2**, **MPh**−**C4,** and **MPhS**−**C6**, respectively; the

corresponding increment in out of plane (OOP) direction is 0.46, 3.58 and 10.23 Å. Obviously, the unchanged CCLs for **MPhS−C2** indicate its most aggregation−insensitive to TA, and **MPhS−C4 and MPhS−C6** are in sequence. The TA has decremental effects on CCLs with shortened end−capped alkyl chains, which is consistent with the broadened and red−shifted absorption spectrum of the annealed **MPhS−C6** film (**Figure S5a** in SI). Consequently, the hole mobility (μ_h) for **MPhS-C6** reaches a maximized value of $1.66\times10^{-3}\,cm^2V^{-1}s^{-1}$, and **MPhS−C4** obtains a minimized μ_h of $1.92\times10^{-4}\,cm^2V^{-1}s^{-1}$, and the μ_h of **MPhS−C2** is in between with a value of $3.71\times10^{-4}\,cm^2V^{-1}s^{-1}$ (**Figure 2b**). The above results demonstrated that **MPhS−C2** featured aggregation-least packing due to its TA− insensitive aggregation; however, its condensed π–π stacking leads to moderate hole mobility, which is an absolute advantage over other aggregation-less materials.

Ultraviolet photoelectron spectroscopy (UPS) measurement is used to validate the shortened end−capped alkyl chains decrease the aggregation sensitivity to TA, and especially suppress the upshifts of the highest occupied molecular orbital (HOMO) energy levels. The HOMO energy levels of the pristine films with/without TA (115°C/10min) were measured, and their shifts were calculated as shown in **Figures 2c**–**d**. Without annealing, the three donors exhibit similar HOMO energy levels of −5.24 eV. Although the HOMO energy levels are slightly upshifted than that measured by CV, the three materials show similar values whether calculated from UPS or CV. However, after TA, the disparity of HOMO energy levels for the three materials has been widened markedly. Thereinto, the HOMO energy level of **MPhS−C6** upshifts to −5.14 eV, with a remarkable change of 0.1 eV; As for **MPhS−C4** and **MPhS−C2**, their HOMO energy level upshifts to −5.19 and −5.23 eV, with an increase of 0.05 eV and 0.01 eV, respectively. Hence, shortening the end-capped acceptor suppressed the HOMO upshifts to TA efficiently.

From the above analysis, shortening the end-capped alkyl chains from hexyl to ethyl realizes our initial molecular design (**Figure 2e**), including: 1) high miscibility during film formation and

aggregation−insensitivity to TA, which potentially ensures a small phase separation; 2) relatively small π−π stacking distance (3.47 Å), which leads to moderate hole transportability even with the lowest ordering; 3) aggregation−insensitivity to TA suppress upshifts of HOMO energy level during TA, which will be helpful to gain a small ΔV_{nr}.

2.2 Device fabrication and characterization

To investigate the photovoltaic performance of three donors by using BTP−eC9 as the acceptor, conventional devices with a structure of ITO/poly(3,4−ethylenedioxythiophene): polystyrene−sulfonate (PEDOT: PSS)/active layer/ PNDIT−F3NBr/Ag were fabricated (**Figure 3a**). The ratios of donor−to−acceptor, TA temperatures, additives, and solvent vapor annealing (SVA) were optimized to improve the device performance (**Tables S4**−**7** in the Supporting Information). Impressively, the optimized device based on **MPhS**−**C2**/BTP−eC9 shows a remarkable PCE of 16.54% with an excellent V_{oc} of 0.886V and J_{sc} of 26.86 mA cm^{-2}, and a reasonable FF of 69.5%. After adding 0.25% DIO and further optimizing the film thickness by solution concentration and spin-coating speed, the PCE was improved to 17.11% with almost unchanged V_{oc} (0.888V) and J_{sc} (26.62 mA cm^{-2}), but an enhanced FF of 72.4%. The obtained PCE and V_{oc} are the highest values for ASM−OSCs to date, which are also comparable to that of polymer OSCs (PSCs). For devices based on **MPhS**−**C4**/BTP−eC9, the best PCE is 15.73%, with a V_{oc} of 0.873 V, a J_{sc} of 25.61 mA cm^{-2}, and an FF of 70.3%. For devices based on **MPhS**−**C6**/BTP−eC9, the best PCE was 16.20%, with a V_{oc} of 0.840V, a J_{sc} of 25.49 mA cm^{-2}, and an FF of 75.6%. The detailed parameters of the best photovoltaic are summarized in **Table 1**. The best *J*−*V* curves and their corresponding external quantum efficiency (EQE) curves, together with the statistical distributions of the best PCEs (*ca.* 20 pieces) for **MPhS**−**C2**/BTP−eC9 with/without DIO, are shown in **Figures 3b**−**d**. The EQE curves for **MPhS**−**C2**/BTP−eC9 and **MPhS**−**C2**/BTP−eC9/DIO almost equal each other, and are higher than the

other two systems in the whole acceptor and the anterior portion of the donor absorption range. This could be attributed to a higher absorption coefficient of **MPhS**−**C2**/BTP−eC9 resulting from the higher absorption coefficient of **MPhS−C2** (**Figures S5b**−**c**), and their efficient charge generation due to their small domain size with long exciton lifetime (will be analyzed below). Noteworthy, the calculated J_{sc} from the EQE is consistent with that measured from the *J*−*V* tests within an error of 2.5%.

In contrast to the devices based on the other two small donors, the highlight of the **MPhS**−**C2**/BTP−eC9 and **MPhS**−**C2**/BTP−eC9/DIO is their simultaneous high V_{oc} and J_{sc}. In the following, we will focus on investigating the reasons for its synchronous high J_{sc} and V_{oc} of **MPhS**−**C2**/BTP−eC9, besides the apparent deviation of FF for the four systems.

The reliance of V_{oc} and J_{sc} values on illumination light intensity is widely applied to distinguish the trap−assisted recombination mechanism versus the bimolecular mechanism (**Figures 3e**−**f**). They are judged by the parameters of ideality factor *n* and α extracted from their fitting curves, where $V_{oc} \propto nkT/q\ln(P)$ and $J_{sc} \propto P^{\alpha}$, in which k is Boltzmann's constant, T is temperature, q is the elementary charge, and *P* is the light intensity. With end-capped alkyl chains increased from ethyl to butyl to hexyl, the n values were more deviation from 1 and increased from 1.05 to 1.08 to 1.19; nevertheless, the corresponding α values were closer to 1, from 0.950 to 0.989 to 0.994. Hence, the longer the end−capped alkyl chains, the more severe trap−assisted monomolecular recombination and the less bimolecular recombination were observed. The photocurrent is limited by monomolecular recombination, and trap-assisted monomolecular recombination was reported as an important loss mechanism.[34] Hence, compared to the other two systems, the reduction in trap−assisted recombination for **MPhS**−**C2**/BTP−eC9 should also contribute to their higher J_{sc}, which is probably attributed to its less interfacial traps resulting from its narrow energy levels broadening because of its TA− insensitive aggregation;[35, 36] however, its relative severe bimolecular

recombination should be responsible for its smaller FF. For **MPhS**−**C2**/BTP−eC9/DIO, the calculated n value slightly decreases from 1.05 to 1.02; however, the α value remarkably increases from 0.950 to 0.993, which well explains its improvement in FF.

2.3 Morphology, charge properties, FF and *J*sc

The variation of FF and J_{sc} couldn't be separated from efficient charge transport and charge generation, both of which are largely dependent on their morphologies.

2.3.1 Molecular packing, charge properties, and FF

Although the three donors exhibit edge−on packing modes preferentially, they are all induced into face−on packing in the blends (**Figures s6**−**7**). Since donors and acceptors have similar d−spacing in the π-π direction (*ca.* 3.45−3.60 Å), the (010) peak in the OOP direction should be a combined peak of them (**Table S8**). However, their characteristic (100) peak could be used to independently evaluate the crystalline ability of the donor (*ca*. 0.28 Å) and the acceptor (*ca*. 0.39 Å), and **Figure 4a** presents the CCL sensitivity to annealing for the donor and acceptor in blends, respectively.

For the blend films without annealing, the three donors have no significant difference in crystallinity as deduced from their similar CCL (around 95 Å) of (100) peak in the IP direction. After TA, the CCLs of (100) peaks increase obviously for both donor and acceptor (Table **S8** and Figure S7); although the increments of acceptor crystallization are similar (*ca.* 23 Å in CCL, **Figure 4a**), the increments of donor crystallization are quite different, and their CCLs of (100) increase by 59 Å, 78 Å and 80 Å for **MPhS**−**C2**/BTP−eC9, **MPhS**−**C4**/BTP−eC9, and **MPhS**−**C6**/BTP−eC9, respectively (**Figure 4a**). Especially, **MPhS**−**C6**/BTP−eC9 presents a new strong packing peak at q=1.35 $Å^{-1}$, which was

consistent with pristine **MPhS**−**C6** molecular packing after annealing, inferring its unique but strong crystalline ability (Figure S7).

After adding DIO in **MPhS**−**C2**/BTP−eC9 blends without annealing, the crystalline ability of both the donor and acceptor were largely improved, indicated by the CCL of (100) peak increases from 96.7 Å to 120.1 Å for the donor and from 48.8 Å to 69.2 Å for the acceptor. Hence, DIO probably changed the molecular interaction between **MPhS**−**C2** and BTP−eC9, and ultimately, their film formation kinetics and molecular packing. Noteworthy, after DIO addition for **MPhS**−**C2**/BTP−eC9, both the CCLs of donor and acceptor exhibited a decreased dependence on TA, and their increments were only 42 Å and 5 Å for the donor and acceptor, respectively (**Figure 4a**). The above result demonstrated that DIO addition not only retained TA− insensitivite aggregation of **MPhS-C2**, but also exhibited the least aggregation sensitivity to TA in the four systems, further reducing ΔV_{nr} through TA channel, which will be further analyzed in the energy loss section. Consistent with the annealed pristine films, the *d*−spacing of π−π stacking for **MPhS**−**C2**/BTP−eC9 was much smaller (3.49 Å) than that of **MPh4**−**C2/**BTP−eC9 (3.57 Å) and **MPhS**−**C6**/BTP−eC9 (3.54 Å). Interestingly, DIO addition further decreased its *d*-spacing of π−π stacking to 3.43 Å, and such a small *d*−spacing was rarely observed in photovoltaic materials. The smaller π−π stacking in **MPhS**−**C2**/BTP−eC9 with/without DIO would benefit its charge transport.

With prolonged end−capped alkyl chain length, the electron mobility (μ_e) decreased while the μ_h of the blends increased (**Figure 4c**). The variation of μ_e was a joint effect of π−π stacking distance and blocking barrier formed by the donors due to their similar crystallinity as deduced from their slightly fluctuated CCLs. Consequently, **MPhS**−**C2**/BTP−eC9 with/without DIO with aggregation−less donor packing and closer π−π stacking exhibited the top two μ_e. Nevertheless, compared to **MPhS**−**C4**, owing to more condense π−π stacking of **MPhS**−**C2**, although its CCL was much smaller, however, the μ_h of **MPhS**−**C2** was still above 10^{-4} $cm^2 V^{-1} s^{-1}$ and quite close to that of **MPhS**−**C4**. This

is the whole situation after DIO addition, with a smaller CCL but much tighter π−π stacking, the μ_h for **MPhS**−**C2**/BTP−eC9/DIO was improved to 3.28×10^{-4} $cm^2 V^{-1} s^{-1}$, which was higher than that of **MPhS**−**C4**/BTP−eC9 (2.81×10^{-4} $cm^2 V^{-1} s^{-1}$). In comparison to **MPhS**−**C2**/BTP−eC9, the DIO addition enhances μ_h due to its slightly improved crystallinity and reduced π−π stacking. With the μ_h gradually improved from **MPhS**−**C2**/BTP−eC9 to **MPhS**−**C4**/BTP−eC9 to **MPhS**−**C2**/BTP−eC9/DIO to **MPhS**−**C6**/BTP−eC9, the charge carrier lifetime increased from 3.52 to 5.12 to 5.40 to 5.88 us, and charge extraction time decreased from 0.43 to 0.4 to 0.39 to 0.34 us as calculated from their transient photovoltage (TPV) and transient photocurrent (TPC) results (**Figure S8**). Furthermore, the increasing trend of μ_h was also consistent with their decreased bimolecular recombination, as we analyzed before. Consequently, the FF correspondingly ameliorated from 69.5% to 70.3% to 72.4% to 75.6%. Hence, a further breakthrough in the device performance of **MPhS-C2**/BTP-eC9/DIO will be possible if we continue to enhance the μ_h of its blend.

2.3.2 Phase separation, exciton lifetime, charge generation and J_{sc}

As we mentioned above, the strong miscibility between the **MPhS**−**C2** and BTP−eC9 during film formation, and the TA− insensitivite aggregation of **MPhS**−**C2** would ensure a small phase separation in **MPhS**−**C2**/BTP−eC9 blends. Transmission resonant soft X−ray scattering (R−SoXS) measurement was performed to quantitative their phase separation. The Lorentz-corrected R−SoXS scattering profiles were analyzed at a photon energy of 284.8 eV (**Figure 4d and Figure S9**) due to their high scattering intensities and obvious peaks for all the blends. Using Lorentz function fitting, **MPhS**−**C6**/BTP−eC9 exhibited a bimodal size distribution with domain sizes at 83 and 42 nm, respectively. However, all other optimized blends were fitted better by the single Log−normal function. Therefore, the **MPhS**−**C6**/BTP−eC9 was also fited by the single Log−normal function to make a more accurate comparison with other systems. With shortened end−capped alkyl chains of

donors, their long period gradually decreases; and they are 32.6, 35.1, 44.7 and 45.2 nm for **MPhS**−**C2**/BTP−eC9, **MPhS**−**C2**/BTP−eC9/DIO, **MPhS**−**C4**/BTP−eC9 and **MPhS**−**C6**/BTP−eC9, respectively. For **MPhS**−**C2**/BTP−eC9 systems, whether with/without DIO, the domain size was much smaller than the other two systems, consistent with the result from atomic force microscope (AFM) height images, transmission electron microscope (TEM) images (**Figure S10**) and its aggregation−less packing. The reason for a still small domain size for **MPhS**−**C6/BTP**−**eC9** with highly molecular packing ability, we had elucidated detailly in our previous work.[25] Based on the assumption of a two−phase morphology, the average domain size was approximately half of the long period.[37] Hence, for **MPhS**−**C2**/BTP−eC9 with/without DIO, the domain size (*ca.* 16−18 nm) quite approaches the general exciton diffusion length (*ca.* 10 nm), which is an overwhelming advantage for efficient charge generation. Additionally, we apply Grazing−Incidence Small−Angle X−ray Scattering (GISAXS) to coarsely evaluate the TA−insensitivity effect on the domain size increments during TA (**Figure S11**). The domain size with annealed film is in good accordance with the results characterized by R−SoXS. Compared the increased domain size during TA, **MPhS**−**C2**/BTP−eC9/DIO owns the smallest one (19.5 nm), while **MPhS**−**C6**/BTP−eC9 exhibits the largest one (39.6 nm), further confirming the TA−intensitivity property of **MPhS**−**C2** effectively decreases the increment of domain size during thermal post−treatment, and ultimately leading to a smaller domain size in **MPhS**−**C2**/BTP−eC9 optimized films.

Shortening alkyl chains were also reported to impact the exciton lifetime,[38] which is also important to exciton dissociation. Time-resolved photoluminescence (TRPL) was applied to measure the exciton lifetime of the small donors (**Figure 4e)**. All the curves were well fitted by the double-exponential decay function, and the detailed data are summarized in **Table S9** in SI. The averaged exciton lifetime was 427, 356, and 417 ps for **MPhS**−**C2**, **MPhS**−**C4**, and **MPhS**−**C6**, respectively. Obviously, the longer exciton lifetime of **MPhS**−**C2** and **MPhS**−**C6** would facilitate their efficient charge generation.

The charge generation efficiency was characterized by the relationship between the photocurrent density (J_{ph}) versus the effective voltage (V_{eff}) (**Figure 4f**); thereinto, J_{ph} represents the current densities difference between illumination (J_L) and dark (J_D), respectively, and V_{eff} represents the voltage differences between the applied bias (V) and the voltage when the photocurrent is zero (V_0). At sufficiently high V_{eff}, all excitons are assumed to be dissociated into free charges, and the photo−generated current reaches the maximum saturation J_{sat}. The exciton dissociation efficiencies (η_{diss}= J_{ph} /J_{sat}) of four systems under short circuit current were calculated to be 0.985, 0.972, 0.964, and 0.977 for the devices based on **MPhS**−**C2**/BTP−eC9, **MPhS**−**C2/**BTP−eC9/DIO, **MPhS**−**C4**/BTP−eC9 and **MPhS**−**C6**/ BTP−eC9, respectively. The more efficient η_{diss} for **MPhS-C2** should be a synergistic effect of its smaller phase separation and longer exciton lifetime at a quite small energy loss. On the contrary, compared to **MPhS**−**C6**, the shorter exciton lifetime of **MPhS**−**C4** rather than its domain size was responsible for its relatively poorer exciton dissociation. Hence, the remarkable J_{sc} of **MPhS**−**C2**/BTP−eC9 with/without DIO should be a synergistic effect of its tight packing and efficient exciton dissociation.

2.4 Relationship among TA, D:A ratios, EQE_{EL} and ΔV_{nr}

2.4.1 TA−aggregation−insensitivity effects on energy loss and ΔV_{nr}

The detailed energy losses were investigated, and the data are summarized in **Table 2**. As shown in **Figure 5a**, the EQE_{EL} value of **MPhS**−**C2**/BTP−eC9 with/without DIO is 8.97×10^{-4} and 6.02×10^{-4}, both of which is almost one order magnitude higher than that of **MPhS**−**C4**/BTP-eC9 (1.5×10^{-4}) and **MPhS**−**C6**/BTP−eC9 (7.5×10^{-5}), and their corresponding eΔV_{nr} values are 0.182, 0.192, 0.228 and 0.247 eV for **MPhS**−**C2**/BTP−eC9, **MPhS**−**C2**/BTP−eC9/DIO, **MPhS**−**C4**/BTP−eC9 and **MPhS**−**C6**/BTP−eC9, respectively. Obviously, the much-enhanced EQE_{EL} and suppressed eΔV_{nr} should

be the major contributors to the V_{oc} increase and low energy loss (0.497 eV, Table 2) in the **MPhS**−**C2**/BTP−eC9 based device.

The V_{oc} of PM6/BTP−eC9 was reported to be only 0.839 V,[39] which is much lower than that of **MPhS**−**C2**/BTP−eC9 device. Hou et al. reported that employing high luminescent polymers is an effective method to decrease the ΔV_{nr}.[40] However, all the pristine donor films exhibit EQE_{EL} almost two orders of magnitude lower than that of blend film in our system, which certainly is not the reason for the low ΔV_{nr} for **MPhS**−**C2**/BTP−eC9 (**Figure S12**).

It is our original material design to gain TA−insensitive aggregation through shortening the end−capped alkyl chains, aiming to reduce ΔV_{nr} during post−treatment. To further confirm the low ΔV_{nr} of **MPhS**−**C2**/BTP−eC9 with/without DIO resulted from its decreased loss during post−treatment, TA effects on V_{oc} and ΔV_{nr} were investigated. Since the device performances without annealing are pretty unstable, to accurately measure their differences, we started by annealing at a low temperature of 65 °C. With annealing temperature increased from 65, 85, 105 to 115 °C, all the V_{oc} based on small donors/BTP−eC9 gradually reduced (**Figure S13** and Tables S4−6). As shown in **Figure 5b**, the decreased V_{oc} after annealing synchronized in their increased ΔV_{nr}; thereinto, the V_{oc} or ΔV_{nr} of **MPhS**−**C2**/BTP−eC9/DIO presented the maximized tolerance to TA, and then **MPhS**−**C2**/BTP−eC9, **MPhS**−**C4**/BTP−eC9, **MPhS**−**C6**/BTP−eC9 in order, which absolutely coincided with their gradually aggregation−sensitivity to TA as we analyzed in the molecular packing section. Interestingly, the EQE_{EL}s at 65°C for all the blends without DIO surpass 10^{-3} (**Figure S14**), corresponding to an ultra−low and nearly the same ΔV_{nr} with a value of *ca.* 160 mV, which we will further analyze in the following section. Obviously, it was the TA (device optimization) that led to their variation of ΔV_{nr} for the three blends without DIO.

Figure 5c shows the HOMO energy level (measured from UPS, **Figure S15**) of the blend at 65°C and 115°C. With the intensified aggregation TA−insensitivity, HOMO level upshifts decreased, which

was in good accordance with the reduced ΔV_{nr}. This varied trend was similar to their pristine films but with an increase in the magnitude of change, which was consistent with their enlarged CCL increments in blend films. Since CT states of all the blends are buried in the pristine BTP-eC9 states, as measured by a combination of sensitive EQE (FTPS−EQE) and electroluminescent spectrum (EL) (**Figure S16**), we also evaluated the CT states from UPS by the function: $IP_D - EA_A \approx HOMO_D - HOMO_A + E_g$, in which IP_D is the ionic potential of the donor in the blend, EA_A is the electron affinity of the pristine acceptor, $HOMO_D$ and $HOMO_A$ are the energy level measured from UPS (Figure S14), and E_g is the energy bandgap measured from CV.[36, 41, 42] As shown in **Figure 5d**, with the depressed TA−insensitive aggregation, the E_{CT} values are decreased from 1.140 to 1.138 to 1.084 to 1.042 eV for optimized annealed **MPhS**−**C2**/BTP−eC9, **MPhS**−**C2**/BTP−eC9/DIO, **MPhS**−**C4**/BTP−eC9 and **MPhS**−**C6**/ BTP−eC9 blends, respectively; and their corresponding $\Delta E_{LE\text{-}CT}$ is enlarged from 0.244, 0.246, 0.300 and 0.342eV. Hence, the aggregation−insensitive to the TA of **MPhS**−**C2** leads to the smallest $\Delta E_{LE\text{-}CT}$ to ensure the smallest ΔV_{nr}. Summarily, the TA−insensitive aggregation successfully suppress the HOMO energy level upshifts, leading to a smaller $\Delta E_{LE\text{-}CT}$ and ΔV_{nr}.

2.4.2 EQE_{EL} of the blend surpasses its pristine low bandgap acceptors

To confirm the EQE_{EL} of **MPhS**−**C2**/BTP−eC9 approaches or even surpass the pristine BTP−eC9, the EQE_{EL} of pristine unannealed/annealed BTP−eC9 films was measured (**Figure 5e**), and the corresponding value is 4.76×10^{-4} and 1.09×10^{-4}, respectively. Obviously, through donor design, Obviously, through donor design, the EQE_{EL} of optimized MPhS−C2/BTP−eC9 with/without DIO devices is six to eight times higher than that of its corresponding pristine acceptor. Furthermore, all the EQE_{EL} of the annealed film at 65°C based on the three blends is at least three times that of the unannealed BTP−eC9 (Figure S14).

To further elucidate the essential reasons for the much higher EQE_{EL} of the blend than that of the pristine acceptor, we used polystyrene (PS) as diluents to see whether this phenomenon could be induced by a reduced aggregation−caused quenching (ACQ). As shown in **Figure 5e**, at PS: BTP−eC9 = 1:1, the EQE_{EL} was doubly improved, demonstrating that ACQ was one of the reasons. Inspired by the positive effect of dispersing acceptor on the improvement of EQE_{EL}, we tuned the D:A ratio to coarsely scattering the acceptor to find whether there exists a smaller ΔV_{nr} (**Figure 5f**, **Figure S17** and **Table S10–11**). Surprisingly, changing the D:A ratio from 10:1 to 1:4, the ΔV_{nr} first decreased and then increased, and a minimized ΔV_{nr} existed. As for **MPhS**−**C2**/BTP−eC9, the ratio with minimized ΔV_{nr} (0.182 V) was close to the optimized ratio of the best device performances (1.9:1). While for **MPhS**−**C6**/BTP−eC9, the ratio range (*ca.* 1:2) with minimized ΔV_{nr} (0.216 V) was quite far from the optimized ratio (1.9:1). Consequently, making the minimized ΔV_{nr} precisely close to the optimized device performances would be necessary to reduce ΔV_{nr} and improve the device performance.

However, the EQE_{EL} of annealed **MPhS**−**C2**/BTP−eC9 blends (1:1) were four times higher than that of PS/BTP-eC9 (1:1), indicating some other mechanisms are also responsible for the enhancement of EQE_{EL} of the blends. Because this phenomenon only exists on the very small $\Delta E_{LE\text{-}CT}$ (annealed blends at 65 °C, and **MPhS**−**C2**/BTP−eC9 optimized blends), probably, an encouraging hybridization between triplet CT states and LE states in OSCs blends is formed.[43, 44] In conclusion, the EQE_{EL} of the blend could be much higher than that of the pristine acceptor at a small $\Delta E_{LE\text{-}CT}$, even for the optimized blends, illustrating the importance of finely energy level regulation in the reduction of ΔV_{nr}.

2.5 Discussions on simultaneous low ΔV_{nr} and high device performances

As we analyzed before, all the three devices (without DIO) after annealed at 65°C own a very small ΔV_{nr} of *ca.* 160 mV but with much poorer device performance due to their unsatisfactory FF and J_{sc}, which agrees well with previously reported results with small ΔV_{nr}. To obtain a comparable ΔV_{nr} value of 0.182 V with the optimized MPhS−C2/BTP−eC9 blend, the other two blends need to anneal at *ca.* 85 °C with much unsatisfied efficiency (Tables S4-S6), further demonstrating the importance of small π−π stacking to promote efficient charge transport at an aggregation−less packing. Hence, the small π−π stacking (3.49 Å and 3.43Å for **MPhS**−**C2**/BTP−eC9 with/without DIO blends, respectively) is a decisive factor in obtaining the concurrent low ΔV_{nr} and high device performance. The TA−insensitive aggregation not only suppresses the upshifts of HOMO energy level during TA, but also suppresses the driving force of crystallinity to minimize the phase separation, facilitating small ΔV_{nr} and efficient charge generation. All the above aspects could be obtained through shortening the end−capped alkyl chains, and their effects on the TA−insensitive aggregation and condense packing are well summarized in **Figure 6a**.

As shown in **Figure 6b** and **Table S12**, due to the less investigation of ΔV_{nr} in ASM-OSCs, we summarize the energy loss of ASM−OSCs with PCE>14%, and **MPhS**−**C2**/BTP−eC9/DIO exhibits the highest PCE with an energy loss below 0.5 eV. Furthermore, **MPhS**−**C2**/BTP−eC9/DIO is also one of the few systems that obtain a high PCE (PCE>16%) with a small ΔV_{nr} (<0.2 V) in OSCs (**Figure 6c** and **Table S13**). In addition, the MPhS−C2/BTP−eC9/DIO exhibited a longer T80 lifetime (the time for sustaining 80% of the initial PCE) under thermal heating (65°C in an inert atmosphere) or light soaking (100 mW/cm2 in an inert atmosphere) than that of MPhS−C6/BTP−eC9. The result illustrates that TA−insensitive aggregation and condense packing benefit not only the high device performance but also the long−term stability (**Figure S18**). Furthermore, the thermal stability and photostability of the device based on MPhS−C2/BTP−eC9/DIO could be comparable to or even surpass that of PM6/BTP-eC9, further illustrating the successful material design concept of TA−insensitive aggregation and condense packing. Summarily, condense packing together with TA−insensitive

aggregation is a potential molecular design direction to obtain a record PCE with low ΔV_{nr} and improved stability.

3. Conclusions

By shortening the end−capped alkyl chains of small molecule donors from hexyl to butyl to ethyl, we successfully obtain a unique molecular packing featuring a narrow d-spacing (3.49 Å) in the charge transport direction, a suppressed upshifts of HOMO energy level after TA post-treatment and a small domain size (*ca.* 16 nm) resulted from its TA−insensitive aggregation in **MPhS**−**C2**/BTP−eC9 blend. Hence, a simultaneous high J_{sc} (26.86 mA cm^{-2}) and high V_{oc} (0.886 V) with a PCE of 16.5% and $\Delta V_{nr.}$ of 0.182V is obtained. The DIO addition further modified the interaction of the donor and acceptor, leading to a further condensed π−π stacking distance of 3.43 Å with slightly improved crystallinity and increased TA−aggregation−insensitivity, further promoting an attain of a champion PCE of 17.1% with a V_{oc} of 0.888 V, a J_{sc} of 26.62 mA cm^{-2}, and an FF of 72.4%. Importantly, the EQE_{EL} of **MPhS**−**C2**/BTP−eC9 with/without DIO is 4−7 times higher than that of pristine **BTP**−**eC9**, resulting in small $\Delta V_{nr.}$ of 0.192 and 0.182V respectively, and ultimately a small energy loss of *ca.* 0.497 eV. The **MPhS**−**C2**/BTP−eC9/DIO wins the highest PCE with the smallest energy loss (or ΔV_{nr}) in ASM−OSCs, which is also one of the best in the whole OSCs. Our results demonstrate the importance of donor design in simultaneously obtaining small ΔV_{nr} and efficient charge generation, and a combination of condense molecular packing and TA− insensitive aggregation is an efficient material design direction.

Declaration of interests

The authors declare no competing interests.

Supporting Information

Supplemental information can be found online

Acknowledgements

Zhang. L. L. and Sun. R. contributed equally to the work. The authors are grateful for the financial support provided by the National Natural Science Foundation of China (51973044) and the Youth Innovation Promotion Association, Chinese Academy of Sciences. R−SoXS data was acquired at beamline 11.0.1.2, at the Advanced Light Source, LBNL, which is supported by the Director, Office of Science, Office of Basic Energy Sciences, of the U.S. Department of Energy under Contract No. DE-AC02-05CH11231.

Received: ((will be filled in by the editorial staff))

Revised: ((will be filled in by the editorial staff))

Published online: ((will be filled in by the editorial staff))

References

[1] P. Bi, S. Zhang, Z. Chen, Y. Xu, Y. Cui, T. Zhang, J. Ren, J. Qin, L. Hong, X. Hao, J. Hou, *Joule* **2021**, *5*, 2408-2419.

[2] Y. Cui, Y. Xu, H. Yao, P. Bi, L. Hong, J. Zhang, Y. Zu, T. Zhang, J. Qin, J. Ren, Z. Chen, C. He, X. Hao, Z. Wei, J. Hou, *Adv. Mater.* **2021**, *33*, 2102420.

[3] C. Li, J. Zhou, J. Song, J. Xu, H. Zhang, X. Zhang, J. Guo, L. Zhu, D. Wei, G. Han, J. Min, Y. Zhang, Z. Xie, Y. Yi, H. Yan, F. Gao, F. Liu, Y. Sun, *Nat. Energy* **2021**, *6*, 605-613.

[4] Y. Dong, Y. Zou, J. Yuan, H. Yang, Y. Wu, C. Cui, Y. Li, *Adv. Mater.* **2019**, *31*, 1970371.

[5] Z. Zheng, J. Wang, P. Bi, J. Ren, Y. Wang, Y. Yang, X. Liu, S. Zhang, J. Hou, *Joule* **2022**, *6*, 171-184.

[6] Y. Lin, J. Wang, Z.-G. Zhang, H. Bai, Y. Li, D. Zhu, X. Zhan, *Adv. Mater.* **2015**, *27*, 1170-1174.

[7] C. Yan, S. Barlow, Z. Wang, H. Yan, A. K. Y. Jen, S. R. Marder, X. Zhan, *Nat. Rev. Mater.* **2018**, *3*, 18003.

[8] J. Wang, X. Zhan, *Acc. Chem. Res.* **2021**, *54*, 132-143.

[9] J. Yuan, Y. Zhang, L. Zhou, G. Zhang, H.-L. Yip, T.-K. Lau, X. Lu, C. Zhu, H. Peng, P. A. Johnson, M. Leclerc, Y. Cao, J. Ulanski, Y. Li, Y. Zou, *Joule* **2019**, *3*, 1140-1151.

[10] J. Benduhn, K. Tvingstedt, F. Piersimoni, S. Ullbrich, Y. Fan, M. Tropiano, K. A. McGarry, O. Zeika, M. K. Riede, C. J. Douglas, S. Barlow, S. R. Marder, D. Neher, D. Spoltore, K. Vandewal, *Nat. Energy* **2017**, *2*, 17053.

[11] F. D. Eisner, M. Azzouzi, Z. Fei, X. Hou, T. D. Anthopoulos, T. J. S. Dennis, M. Heeney, J. Nelson, *J. A. Chem. Soc.* **2019**, *141*, 6362-6374.

[12] X.-K. Chen, D. Qian, Y. Wang, T. Kirchartz, W. Tress, H. Yao, J. Yuan, M. Hülsbeck, M. Zhang, Y. Zou, Y. Sun, Y. Li, J. Hou, O. Inganäs, V. Coropceanu, J.-L. Bredas, F. Gao, *Nat. Energy* **2021**, *6*, 799-806.

[13] X.-K. Chen, V. Coropceanu, J.-L. Brédas, *Nat. Commun.* **2018**, *9*, 5295.

[14] A. Classen, C. L. Chochos, L. Lüer, V. G. Gregoriou, J. Wortmann, A. Osvet, K. Forberich, I. McCulloch, T. Heumüller, C. J. Brabec, *Nat. Energy* **2020**, *5*, 711-719.

[15] N. Gasparini, F. V. A. Camargo, S. Frühwald, T. Nagahara, A. Classen, S. Roland, A. Wadsworth, V. G. Gregoriou, C. L. Chochos, D. Neher, M. Salvador, D. Baran, I. McCulloch, A. Görling, L. Lüer, G. Cerullo, C. J. Brabec, *Nat. Commun.* **2021**, *12*, 1772.

[16] Q. Liu, S. Smeets, S. Mertens, Y. Xia, A. Valencia, J. D'Haen, W. Maes, K. Vandewal, *Joule* **2021**, *5*, 2365-2379.

[17] W. Deng, W. Liu, R. Qian, H. Wu, *J. Phy. Chem. Lett.* **2022**, *13*, 544-551.

[18] S. Liu, J. Yuan, W. Deng, M. Luo, Y. Xie, Q. Liang, Y. Zou, Z. He, H. Wu, Y. Cao, *Nat. Photon.* **2020**, *14*, 300-305.

[19] J. Yan, E. Rezasoltani, M. Azzouzi, F. Eisner, J. Nelson, *Nat. Commun.* **2021**, *12*, 3642.

[20] T. Xu, J. Lv, K. Yang, Y. He, Q. Yang, H. Chen, Q. Chen, Z. Liao, Z. Kan, T. Duan, K. Sun, J. Ouyang, S. Lu, *Energy Environ. Sci.* **2021**, *14*, 5366-5376.

[21] M. Jiang, H. Bai, H. Zhi, L. Yan, H. Y. Woo, L. Tong, J. Wang, F. Zhang, Q. An, *Energy Environ. Sci.* **2021**, *14*, 3945-3953.

[22] J. Ge, L. Hong, W. Song, L. Xie, J. Zhang, Z. Chen, K. Yu, R. Peng, X. Zhang, Z. Ge, *Adv. Energy Mater.* **2021**, *11*, 2100800.

[23] L. Nian, Y. Kan, K. Gao, M. Zhang, N. Li, G. Zhou, S. B. Jo, X. Shi, F. Lin, Q. Rong, F. Liu, G. Zhou, A. K. Y. Jen, *Joule* **2020**, *4*, 2223-2236.

[24] D. Deng, Y. Zhang, J. Zhang, Z. Wang, L. Zhu, J. Fang, B. Xia, Z. Wang, K. Lu, W. Ma, Z. Wei, *Nat. Commun.* **2016**, *7*, 13740.

[25] L. Zhang, X. Zhu, D. Deng, Z. Wang, Z. Zhang, Y. Li, J. Zhang, K. Lv, L. Liu, X. Zhang, H. Zhou, H. Ade, Z. Wei, *Adv. Mater.* **2022**, *34*, 2106316.

[26] J. Qin, Z. Chen, P. Bi, Y. Yang, J. Zhang, Z. Huang, Z. Wei, C. An, H. Yao, X. Hao, T. Zhang, Y. Cui, L. Hong, C. Liu, Y. Zu, C. He, J. Hou, *Energy Environ. Sci.* **2021**, *14*, 5903-5910.

[27] Z. Zhang, Q. Wu, D. Deng, S. Wu, R. Sun, J. Min, J. Zhang, Z. Wei, *J. Mater. Chem. C* **2020**, *8*, 15385-15392.

[28] B. Xiao, M. Zhang, J. Yan, G. Luo, K. Gao, J. Liu, Q. You, H.-B. Wang, C. Gao, B. Zhao, X. Zhao, H. Wu, F. Liu, *Nano Energy* **2017**, *39*, 478-488.

[29] J. Xin, X. Meng, X. Xu, Q. Zhu, H. B. Naveed, W. Ma, *Matter* **2019**, *1*, 1316-1330.

[30] Y. Bian, L. Han, C. Han, H. Lin, H. Zhang, J. Bian, L. Dong, *CrystEngComm* **2014**, *16*, 2702-2714.

[31] J. T. Dull, Y. Wang, H. Johnson, K. Shayegan, E. Shapiro, R. D. Priestley, Y. H. Geerts, B. P. Rand, *J. Phy. Chem. C* **2020**, *124*, 27213-27221.

[32] J. A. Baird, B. Van Eerdenbrugh, L. S. Taylor, *J. Pham. Sci.* **2010**, *99*, 3787-3806.

[33] A. A. Boopathi, S. Sampath, T. Narasimhaswamy, *New J. Chem.* **2019**, *43*, 9500-9506.

[34] S. Zeiske, O. J. Sandberg, N. Zarrabi, W. Li, P. Meredith, A. Armin, *Nat. Commun.* **2021**, *12*, 3603.

[35] Q. Bao, O. Sandberg, D. Dagnelund, S. Sandén, S. Braun, H. Aarnio, X. Liu, W. M. Chen, R. Österbacka, M. Fahlman, *Adv. Funct. Mater.* **2014**, *24*, 6309-6316.

[36] C. Wang, F. Moro, S. Ni, Q. Zhang, G. Pan, J. Yang, F. Zhang, I. A. Buyanova, W. M. Chen, X. Liu, M. Fahlman, *Nano Energy* **2020**, *72*, 104677.

[37] K. Jiang, Q. Wei, J. Y. L. Lai, Z. Peng, H. K. Kim, J. Yuan, L. Ye, H. Ade, Y. Zou, H. Yan, *Joule* **2019**, *3*, 3020-3033.

[38] N. A. Tegegne, Z. Abdissa, W. Mammo, T. Uchiyama, Y. Okada-Shudo, F. Galeotti, W. Porzio, M. R. Andersson, D. Schlettwein, V. Vohra, H. Schwoerer, *J. Phy. Chem. C* **2020**, *124*, 9644-9655.

[39] Y. Cui, H. Yao, J. Zhang, K. Xian, T. Zhang, L. Hong, Y. Wang, Y. Xu, K. Ma, C. An, C. He, Z. Wei, F. Gao, J. Hou, *Adv. Mater.* **2020**, *32*, 1908205.

[40] J. Wang, L. Ma, Y. W. Lee, H. Yao, Y. Xu, S. Zhang, H. Y. Woo, J. Hou, *Chem. Commun.* **2021**, *57*, 9132-9135.

[41] Z. Guan, H.-W. Li, Y. Cheng, Q. Yang, M.-F. Lo, T.-W. Ng, S.-W. Tsang, C.-S. Lee, *J. Phy. Chem. C* **2016**, *120*, 14059-14068.

[42] P. Wan, X. Chen, Q. Liu, S. Mahadevan, M. Guo, J. Qiu, X. Sun, S.-W. Tsang, M. Zhang, Y. Li, S. Chen, *J. Phy. Chem. Lett.* **2021**, *12*, 10595-10602.

[43] A. J. Gillett, A. Privitera, R. Dilmurat, A. Karki, D. Qian, A. Pershin, G. Londi, W. K. Myers, J. Lee, J. Yuan, S.-J. Ko, M. K. Riede, F. Gao, G. C. Bazan, A. Rao, T.-Q. Nguyen, D. Beljonne, R. H. Friend, *Nature* **2021**, *597*, 666-671.

[44] L. Baisinger, J. M. Andrés Castán, P. Simón Marqués, G. Londi, C. Göhler, C. Deibel, D. Beljonne, C. Cabanetos, P. Blanchard, J. Benduhn, D. Spoltore, K. Leo, *ChemSusChem* **2021**, *14*, 3622-3631.

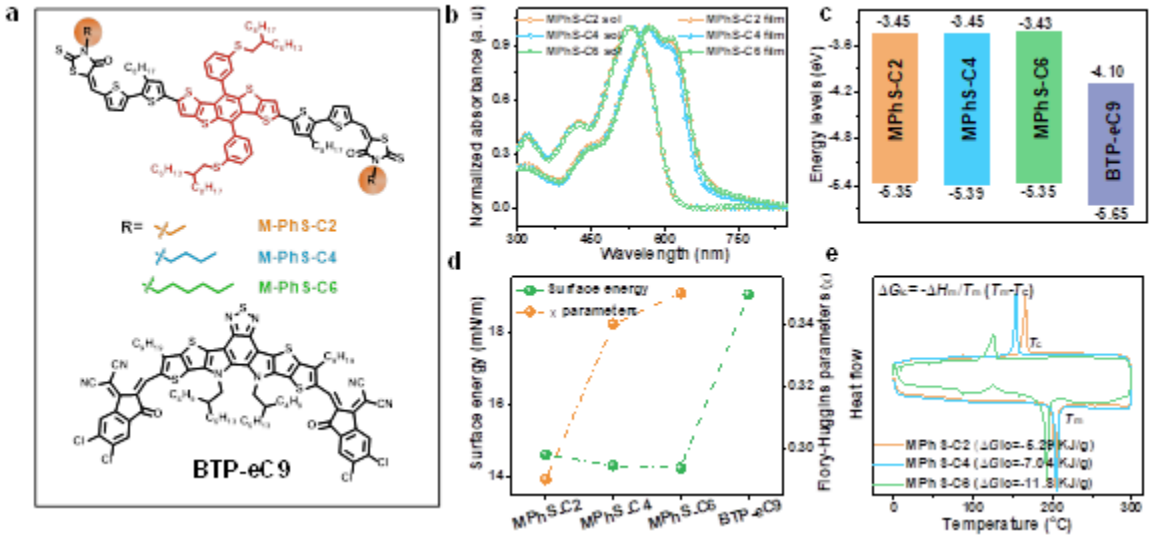

Figure 1. Molecular properties. a) molecular structures; b) absorption spectrum in CF solution and solid film; c) energy alignments measured by CV; d) surface energy and calculated Flory–Huggins parameters; e) the driving force for molecular packing ability calculated from DSC curves.

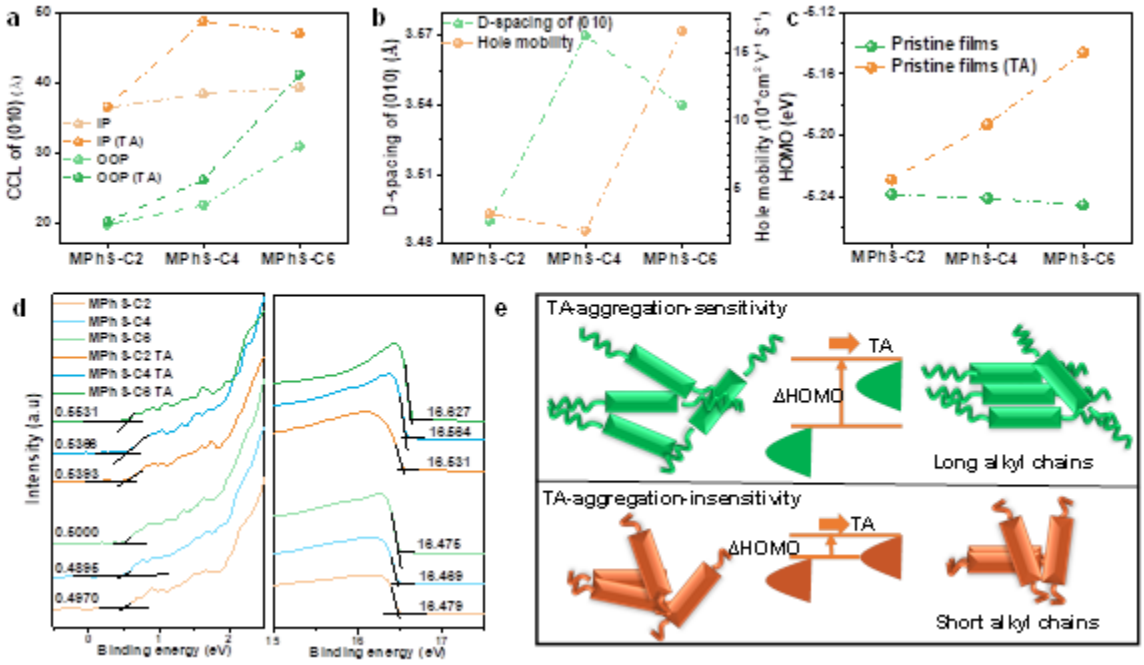

Figure 2. The sensitivity of pristine molecular packing and upshifts of HOMO to TA.a) CCL sensitivity to TA calculated from GIWAXS b) d-spacing calculated from GIWAXS for the annealed films; c) HOMO energy levels for small donors with/without annealing;d) UPS curves for small donors with/without annealing; e) Schemes of end-capped alkyl chains effect on the TA sensitivity of molecular packing and upshifts of HOMO energy levels.

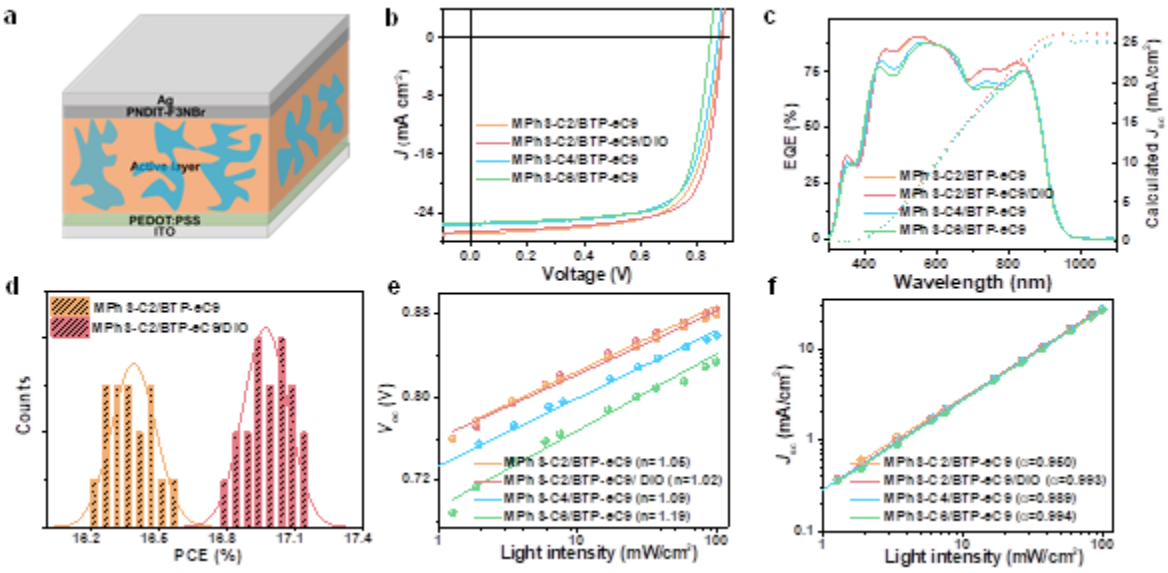

Figure 3. Device performances. a) device structure; b) *J*–*V* curves of best devices; c) corresponding EQE of b); d) Statistical distribution of best PCE for MPhS–C2/BTP–eC9 with or without DIO ≈20 pieces; e) V_{oc} dependent on incident light intensity; f) J_{sc} dependent on incident light intensity

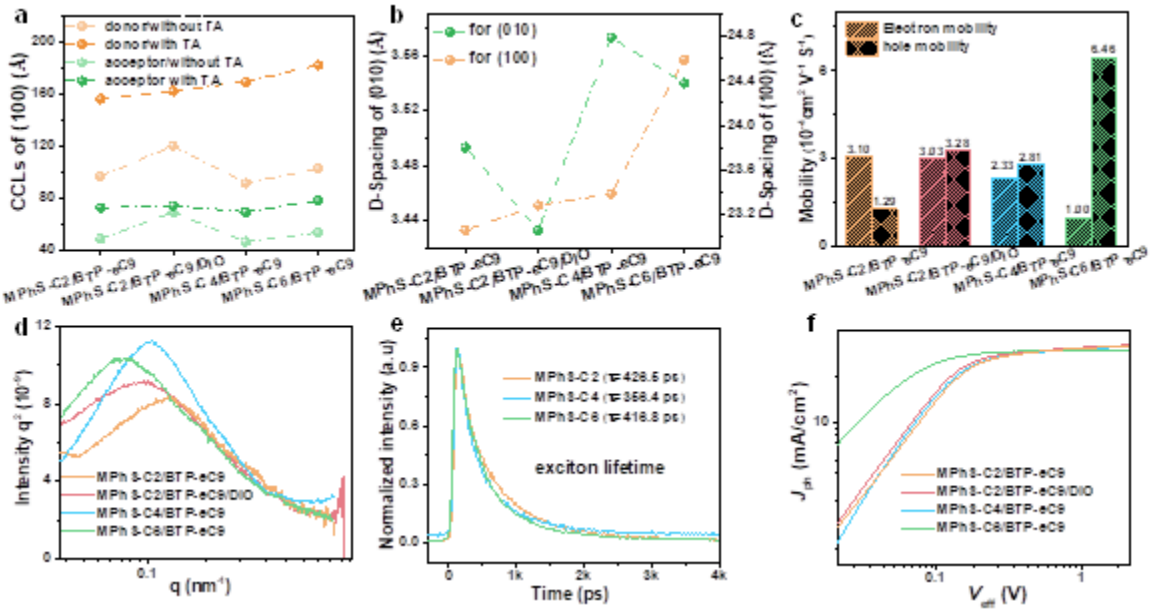

Figure 4. Morphology, charge transport and generation.a) crystallinity sensitivity of donors and acceptors to TA, represented by their CCLs; b) D-spacing calculated from GIWAXS; c) hole and electron mobility in the optimized blend; d) R−SoXS curves; e) exciton lifetime of the three donors; f) Charge generation characterized by the relationship between V_{eff} and J_{ph}.

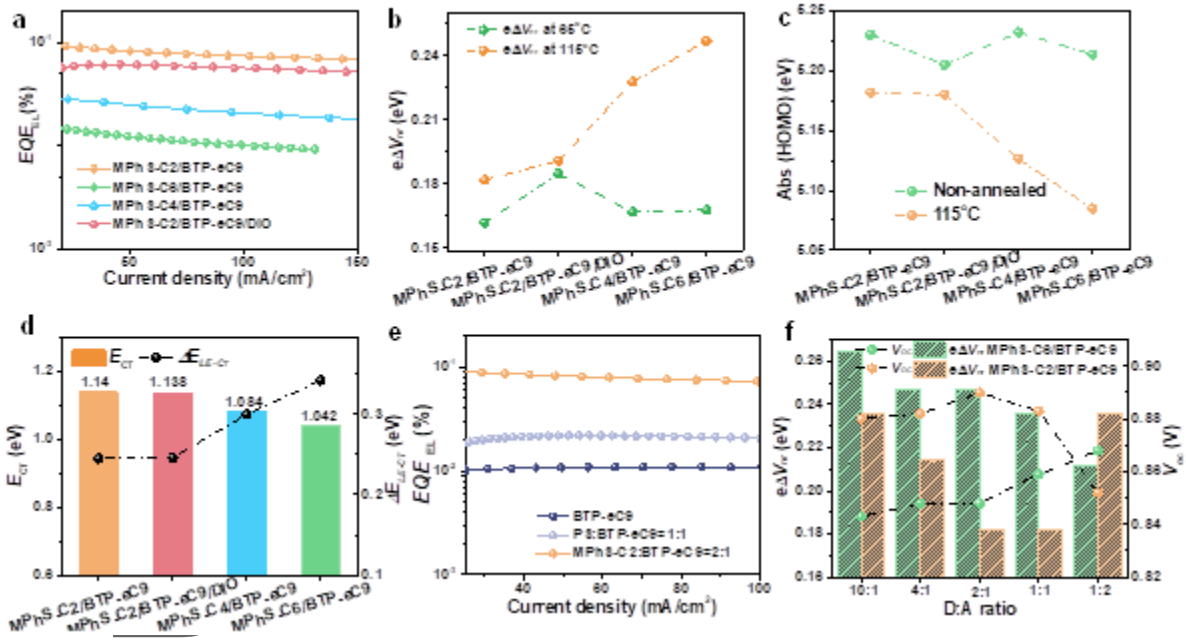

Figure 5. Energy loss and $\Delta V_{nr.}$ a) EQE_{EL} for optimized devices; b) the ΔV_{nr} sensitivity to TA; c) the upshifts sensitivity of HOMO energy levels of the blends to TA; d) E_{CT} and $\Delta E_{LE\text{-}CT}$ calculated from UPS; e) EQE_{EL} comparisons between OSC blends and annealed/PS diluted annealed pristine acceptors;f) ΔV_{nr} and V_{oc} variation with D:A ratios based on MPhS−C2/BTP−eC9 and MPhS−C6/BTP−eC9.

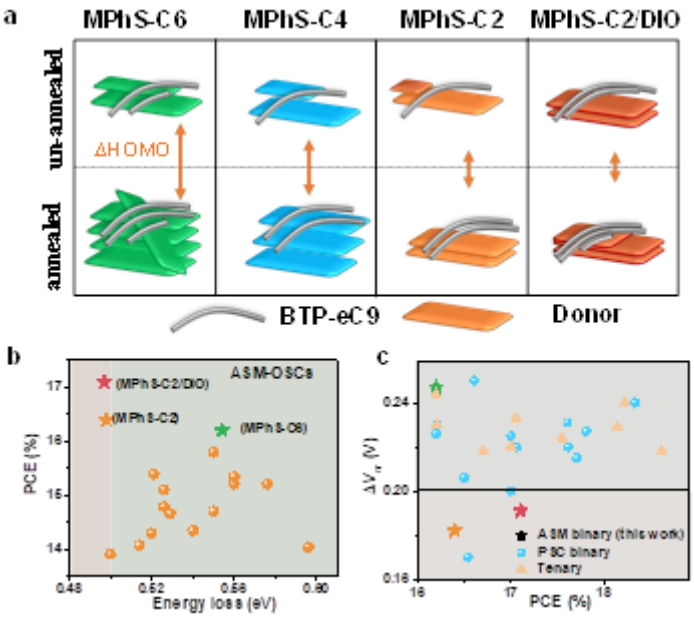

Figure 6. Simultaneous low energy loss and high device performances. a) Summary diagram of the shortening end-capped alkyl chains effects on TA−aggregation−insensitivity and condense packing; b) Summary of energy loss and device performance with PCE>14% in ASM−OSCs; c) Summary of ΔV_{nr} and device performance with PCE>16% in OSCs.

Table 1. Detailed device parameters of optimized devices

Active layer	TA^c [°C]	V_{oc} [V]	J_{SC} [mA cm^{-2}]	J_{SC}^{EQE} [mA cm^{-2}]	FF [%]	PCE (%) Best	PCE (%) Average [b]
MPhS−C2:BTP−eC9	115	0.886	26.86	26.20	69.52	16.54	16.38±0.09
MPhS−C2:BTP−eC9[a]	115	0.888	26.62	26.12	72.38	17.11	16.97±0.10
MPhS−C4:BTP−eC9	115	0.873	25.61	25.30	70.28	15.73	15.63±0.13

MPhS−C6:BTP−eC9	115	0.840	25.49	25.00	75.60	16.20	16.05±0.12

[a] with 0.25% DIO ;

[b] averaged from the top best 10 devices;

[c] thermal annealing (TA) at the temperature for 10 min.

Table 2 Summarized energy loss data based on optimized devices

Active blends	E_g [eV]	$\Delta E1$[a] [eV]	$\Delta E2$[b] [eV]	$\Delta E3$[c] [eV]	eV_{oc}[d] [eV]	ΔE_{loss} [eV]
MPhS−C2 /BTP−eC9	1.384	0.26	0.056	0.182	0.886	0.498
MPhS−C2/BTP−eC9/DIO	1.384	0.26	0.047	0.192	0.887	0.497
MPhS−C4/BTP−eC9	1.384	0.26	0.030	0.228	0.866	0.518
MPhS−C6/BTP−eC9	1.384	0.26	0.038	0.247	0.839	0.545

[a] radiative recombination loss above the bandgap

[b] radiative recombination loss below the bandgap

[c] non-radiative recombination loss below the bandgap ($e\Delta V_{nr}$)

[d] calculated V_{oc} from E_g and energy loss

Table entry

By shortening end-capped alkyl chains from hexyl to ethyl (MPhS-C2), MPhS-C2 features a simultaneous TA–insensitive aggregation and condense packing, leading to a concurrent suppressed upshifts of HOMO energy level during post-treatment, small phase separation and efficient charge ransport at aggregation-less packing in MPhS-C2/BTP-eC9/DIO device, promoting an obtain of the highest PCE of 17.11% with a ΔV_{nr} of 0.192 V in ASM-OSCs.

*Lili Zhang,[#] Rui Sun,[#] Ziqi Zhang, Jianqi Zhang, Qinglian Zhu, Wei Ma, Jie Min, Zhixiang Wei and Dan Deng**

Donor End-capped Alkyl Chain Length Dependent Non-Radiative Energy Loss in All-small-molecule Organic Solar Cells

ToC figure